Al-Nahrain Journal of Science
ANJS, Vol.28 (4), December, 2025, pp. 146-164

Quantum Chemical Insights into the Electronic, Vibrational and Thermodynamic Properties of Chloro-Substituted Anisole

Tulsi Ojha, Prakash Man Shrestha, Suresh Prasad Gupta, Krishna Bahadur Rai*

Department of Physics, Patan Multiple Campus, Patandhoka, Lalitpur Tribhuvan University, Kathmandu, Nepal

Article's Information

Received: 27.05.2025
Accepted: 08.09.2025
Published: 15.12.2025

Keywords:
Anisole,
Density functional theory,
Electronic structure,
Vibrational analysis,
Thermodynamic parameters.

Abstract

Anisole, also known as methoxybenzene, is an organic compound with the formula \(CH_{3}OC_{6}H_{5}\). It is a colorless liquid with a sweet, aromatic odor similar to anise seeds and is used as an intermediate in the synthesis of pharmaceuticals, agro-chemicals, and fragrances. This study is about the quantum chemical insight into the Electronic, vibrational, and thermodynamic properties. The study first analyzed the optimized molecular structures and identified different physical properties. The Non-Co-valent Interactions (NCI)-Reduced Density Gradient (RDG) reveal weak hydrogen bonding and strong repulsive interactions. Molecular electrostatic potential mapping shows higher reactivity in chlorine-substituted anisole, with key reactive sites at oxygen, chlorine, and carbon atoms. Anisole has an excitation energy of 5.770 eV and a lower electronegativity of 3.2850 eV, indicating kinetic stability. Para-chloroanisole (PCA) exhibits the lowest energy gap at 5.481 eV and chemical hardness of 2.7405 eV, suggesting high reactivity. The quantum energy levels are observed in the density of States (DOS) spectrum. Due to their electronegative nature, chlorine atoms show positive charges while oxygen atoms, owing to their electron-withdrawing properties, show negative Mulliken charges, respectively, and serve as key reactive sites. In addition to that, Infrared (IR), Raman, and UV-visible spectra reveal different vibration modes and spectral intensities. Thermodynamic functions such as constant pressure (Cp), enthalpy (H), and entropy (S) for all studied molecules increase with temperature.

http://doi.org/10.22401/ANJS.28.4.12
*Corresponding author: krishna.rai@pmc.tu.edu.np

1. Introduction

Anisole, also known as methoxybenzene or methyl phenyl ether, is an organic compound with the chemical formula $C_6H_5OCH_3$. The methoxy group in an aromatic ring system is an electron-donating substituent. After fluorine, chlorine is the second most electronegative atom among all the compounds. As a result, electrons are drawn to chlorine, lowering the electron density at the carbon in a C–Cl bond. Additionally, due to weak electron-electron repulsion, Cl has a stronger electron affinity than any other halogen. It has been used as an alternative in the manufacture of perfumes and as a flavoring agent [1] for certain foods. It is used to produce perfume, pharmaceuticals, solvents, and dyes, and as an intermediate to manufacture organic compounds [2]. Mono-halogen-substituted. anisole has also been investigated using various experimental techniques such as Fourier transform infrared spectroscopy, resonance-enhanced multiphonic ionization, laser-induced fluorescence, and Mass-Analyzed Threshold Ionization spectroscopy, providing abundant molecular information in the neutral ground, electronic excited, and cation ground states [3]. The photophysical properties of oligo-p-chloro-anisole were reported applying Density Functional Theory (DFT) calculations based on the B3LYP method with

6-31G(d,p) and 3-21G* as basis sets [4]. The spectroscopic properties of anisole in aqueous solution using computational and experimental approaches have been investigated [5]. A DFT method at the B3LYP/6-311G++ level was applied for spectroscopic and structural analysis of P-dimethyl amino azobenzene [6]. Photo absorption studies on anisole were also performed in the UV–Vis region (4.5-11.8 eV) using synchrotron radiation [7]. For these reasons, anisole and its derivatives are important subjects for research. A literature survey reported no detailed quantum chemical investigations for anisole and its chlorine derivatives at ortho, meta, and para positions. Accordingly, the present research is undertaken to study the electronic, vibrational, and thermodynamic properties of the optimal structure of Anisole and its chloro-substituted anisole. For this, we find comparisons of Non-Covalent Interactions (NCI)-Reduced Density Gradient (RDG) analysis, topology (Electron Localization Function (ELF) and Localized Molecular Orbital (LOL)), Molecular Electrostatic Potentials (MEPs), Frontier Molecular Orbitals (FMO), global reactivity descriptors, Density of States (DOS), Mulliken charges, vibrational spectra assignment (IR, Raman, UV-Vis analysis), and thermodynamic parameters with variation in temperature, all reported using DFT/B3LYP/6-31+G(d,p) basis set at gas phase. This study can serve as a method to differentiate between anisole and its chlorine derivatives or to select the appropriate form of anisole and its derivatives for specific applications.

2. Computational Methodology

All quantum chemical calculations were performed on the neutral state without the influence of any solvent (i.e., gas phase) using Gaussian09W [8] and visualized with GaussView 6.0 [9]. We used density functional theory (DFT) [10] with Becke's hybrid functional and the Lee-Yang-Parr correlation (B3LYP), along with a 6-31+G(d,p) basis set [11], to get optimized structures and vibrational spectra of anisole and its ortho, meta, and para chloro derivatives. Thermodynamic properties were derived from Gaussian log files using Moltran software [12], while DOS spectra were generated with GaussSum 3.0 [13]. Non-covalent interactions, LOL, and ELF analyses were conducted using VMD 1.9.4a53 [14] and Multiwfn. UV-Vis spectra were obtained via the TD-DFT method employing a B3LYP functional and a 6-31+G (d,p) basis set in the gas phase.

3. Theory and Formula

To perform the RDG analysis, the following equation gives the mathematical representation of RDG [15] for the molecule,

$$RDG = \frac{1}{2(3\pi^2)^{\frac{1}{3}}}\left|\frac{\nabla\rho(r)}{\rho(r)}\right|^{\frac{4}{3}} \dots (1)$$

In this equation, $\nabla\rho(r)$ represents the gradient of the electron density $\rho(r)$ at a specific position within the molecular structure. The topology study, ELF, and LOL have been performed using Multiwfn 3.8 [16]. The ELF function [17] is defined by the equation as follows

$$ELF = \frac{1}{1+\left(\frac{D}{D_h}\right)^2} \dots (2)$$

With $D = \frac{1}{2}\sum_i|\varphi_i|^2 - \frac{1}{8}\frac{|\nabla\rho|^2}{\rho}$ and $D_h = \frac{3}{10}(3\pi^2)^{\frac{2}{3}}\rho^{\frac{5}{3}}$, where D and D_h represent the excess kinetic energy and the reference value. For the LOL analysis, Schmider and Becke's LOL equations [18] are applied,

$$LOL(r) = \frac{\tau(r)}{1+\tau(r)} \dots (3)$$

Where $\tau(r)$ refers to the dimensionless variable and

$$\tau(r) = \frac{g_0(r)}{g(r)} = \frac{D_0(r)}{\frac{1}{2}\sum_i \eta_i|\nabla\varphi_i(r)|^2} \dots (4)$$

Where g(r) is the electron kinetic energy, φ_i is the Hartree-Fock orbitals, and $D_0(r)$ is the spin-polarized system. MEP sheds light on the distribution of positive and negative charges within molecules and is utilized to show and examine how the electrostatic potential distribution surrounding a molecule is organized.

The molecular electrostatic potential V(r) is produced due to the collective effect of the negative and positive charges corresponding to electrons and nuclei.The expression for estimation of V(r) [19] is,

$$V(r) = \sum_A \frac{Z_A}{|\vec{R}_A - \vec{r}|} - \int \frac{\rho(\vec{r})}{|\vec{r'} - \vec{r}|} \dots (5)$$

Z_A is the charge on nucleus A, present at R_A, and $\rho(r)$ is the electronic density function of the molecule. The highest occupied molecular orbital (HOMO)-lowest unoccupied molecular orbital (LUMO) energy gap and global reactivity parameters have been calculated based on Koopman's closed shell orbit and equations proposed by Parr and Pearson, all in the gas phase [20, 21]. The formulae required for the calculation of parameters, energy gap (ΔE), chemical hardness (η), softness (S), electronegativity (χ), chemical potential (μ), the electrophilicity index (ω) is presented in the equations. Energy gap $(\Delta E) = HOMO - LUMO = I - A$ ... (6)

Where I is the ionization potential and A is the electron affinity of the system.

$$\eta = \frac{\Delta E}{2} \dots (7)$$

$$S = \frac{1}{\eta} \dots (8)$$

$$\chi = -\frac{E_{HOMO} + E_{LUMO}}{2} \dots (9)$$

$$\mu = -\chi \dots (10)$$

$$\omega = \frac{\mu^2}{2\eta} \dots (11)$$

4. Results and Discussion

4.1. Molecular structure with optimization

Figure 1(a), (b), (c) and (d) show the optimized molecular structural geometry with the numbering scheme of (a) anisole, (b) ortho-chloroanisole (OCA), (c) meta-chloroanisole (MCA) and (d) para-chloroanisole (PCA), respectively. For anisole structure, on the aromatic ring, the H atom at C5 is replaced by the oxygen-containing ether group as shown in Figure 1(a). The optimized structure of anisole shows that all ring bonds have partial double-bond character due to electron delocalization caused by the methoxy group (OCH_3), making them neither purely single nor purely double bonds. For other substituents of anisole, the chlorine atom is replaced on the ring of H atom at C4, C3 and C2 at the second, third and fourth positions on the benzene ring so that the molecule becomes 2-chloroanisole (ortho-chloroanisole), 3-chloroanisole (meta-chloroanisole), and 4-chloroanisole (para-chloroanisole) respectively as in Figure 1(b), (c) and (d). After optimization, it is observed that anisole gets optimized in the energy -9437.14 eV. Similarly, OCA, MCA, and PCA get optimized in the energy -21952.91 eV, -21953.84 eV, and -21953.69 eV, respectively.

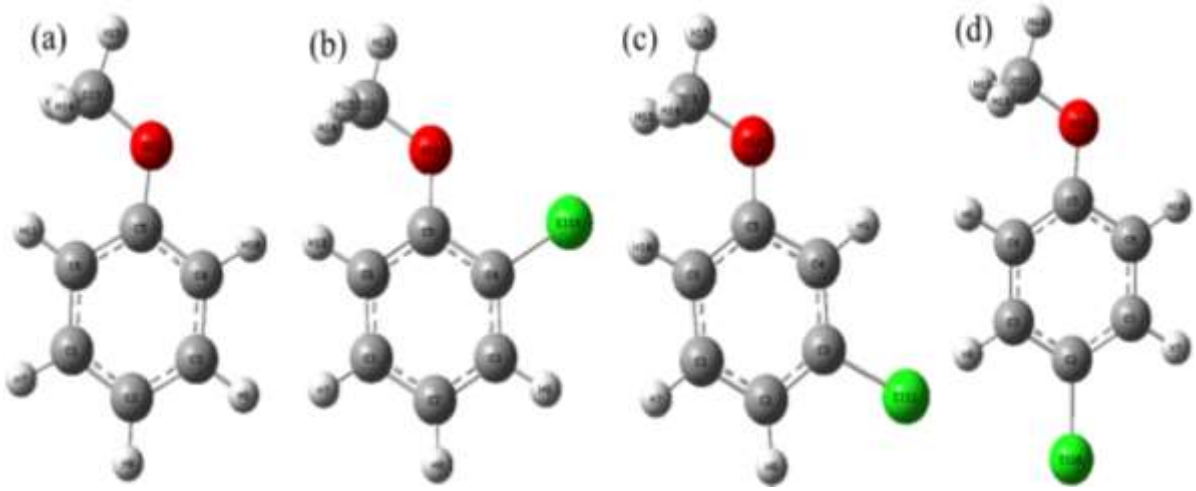

Figure 1. Optimized structure of (a) Anisole, (b) OCA, (c) MCA and (d) PCA

4.2. Non-Covalent Interactions (NCI) and Reduced Density Gradient (RDG) analysis

The Non-Covalent Interactions (NCI) [22] analysis identifies the interactions distinguished by different colors. In Figure 2(a), (c), (e) and (g), the red color disk-shaped blocks (compared with the upper bar) indicate the steric repulsion between the oxygen atoms of the methoxy substituents and within the benzene ring of each of the molecules. These disk-shaped blocks indicate non-covalent interactions; hence, the strong repulsive steric effect is a prime factor in all the molecules. The OCA in Figure 2(c) participates in strong Van der Waals interactions with more area covered by green color disk-shaped blocks. In contrast, the absence of blue blocks suggests a weak H-bond interaction within the studied molecules. In RDG analysis, RDG clusters, their spikes, and λ_2 give information about the type of bond and the strength of the interaction. The relationship between the product of electron density (ρ) and the RDG is shown in Figure 2(b), (d), (f) and (h) based on the second Hessian eigenvalue sign [23]. The graphic representation shows red spikes, green spikes, and no spikes for the blue color, these characteristic spikes and color patterns indicate the existence of van der Waals interactions and steric effects. On the other hand, the lack of blue spikes indicates no hydrogen bond interaction in the molecule. The anisole in Figure 2(b) and the PCA molecule in Figure 2(h) exhibit plenty of red-colored spikes, suggesting a strong repulsive interaction with a larger positive value of λ_2 and a high density. In Figure 2(d), the occupancy of a large area of green-colored RDG scattered points in the OCA

molecule indicates a Van der Waals interaction with a zero value of λ_2 and density. Thus, it is observed that in the RDG study, a strong repulsive steric effect is the dominant interaction in the anisole and PCA compared to the other studied molecules. This is because the chlorine atom in anisole is absent, and the influence of the reactive methoxy group is minimal for PCA [24].

4.3. Electron localization function (ELF) and Local Orbital locator (LOL) analysis These electron localization function (ELF) and local orbital locator (LOL) analysis reveal the molecular surface's atomic shell structure, chemical bonding classification, charge-shift bond verification, lone pairs, and areas of electron delocalization.

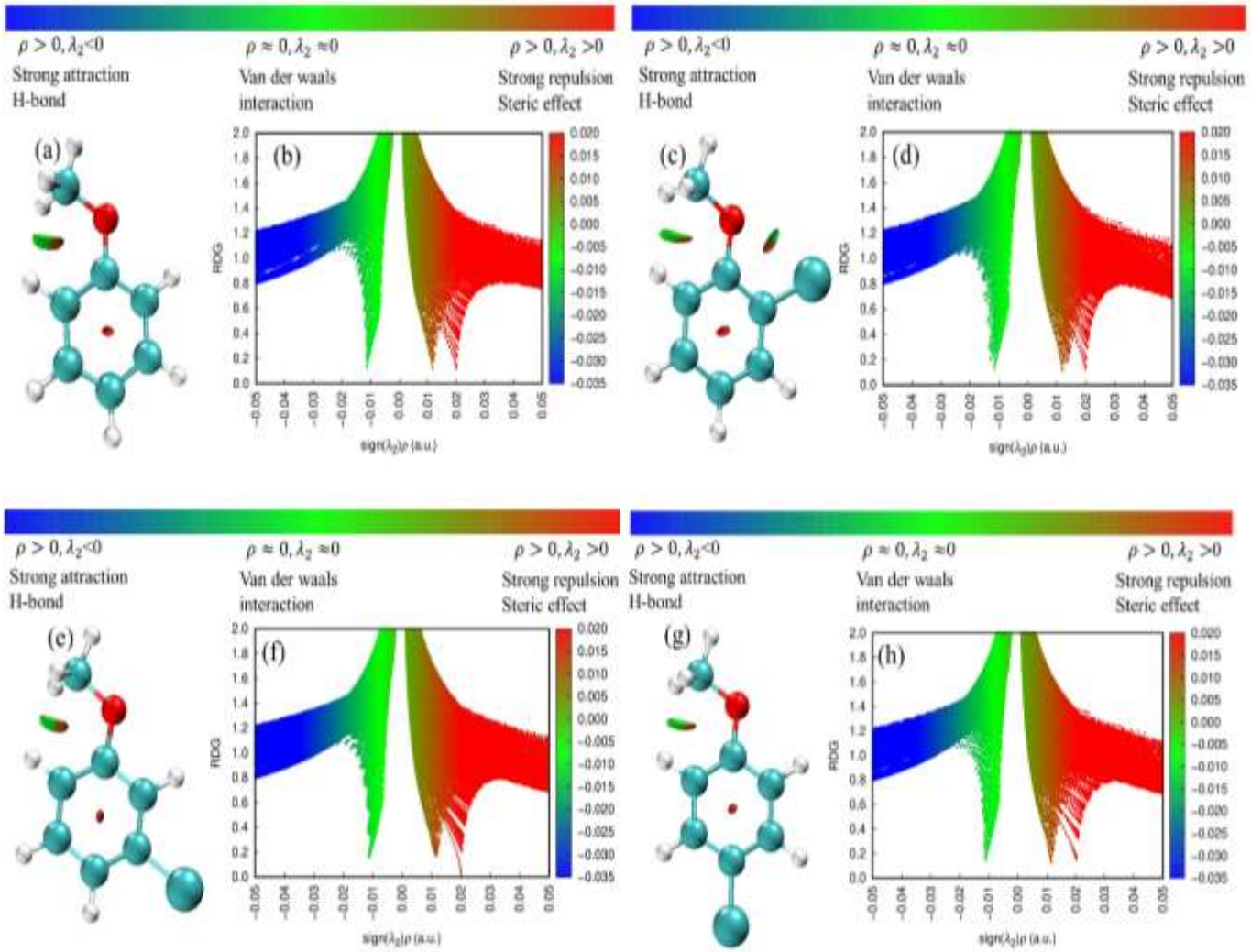

Figure 2. (a) Non-Covalent Interactions (NCI) and (b) RDG scatter plot for anisole, (c) Non-Covalent Interactions (NCI) and (d) RDG scatter plot for OCA, (e) Non-Covalent Interactions (NCI) and (f) RDG scatter plot for MCA and (g) Non-Covalent Interactions (NCI) and (h) RDG scatter plot for PCA

Representations of ELF and LOL are displayed respectively in Figures 3 and 4 for (A) anisole, (B) OCA, (C) MCA, and (D) PCA. The pictorial representations of Figure 3(a) and 4(a) of (A-D) molecules have a shaded surface map with the projection showing an electronic environment highlighting areas of high and low electron density (where electrons are highly localized or delocalized). Figure 3(b) and 4(b) of (A-D) molecules have colored surface identifying degrees of electron localization by assigning gradient colored scale and Figure 3(c) and 4(c) of (A-D) molecules have gradient lines map with contour lines showing the direction and magnitude of increasing or decreasing values of ELF and LOL. While observing ELF in Figure 3(a) and 3(b) for molecules (A-D), lower values (ELF<0.5)

represent locations where electrons are predicted to be delocalized [25] and these are detected around carbon and chlorine atoms in the ring. In contrast, larger values (i.e., ELF [0.5 to 1.0]) indicate that electrons are substantially localized, suggesting the presence of inner shells, a lone pair of atoms, or a covalent link in the region of hydrogen atoms indicated by red color [25]. From Figure 3(c) of molecules (A-D), it can then be inferred that high electron density represented by black color around hydrogen and carbon atoms indicates significant concentration of electrons, revealing that the electrons in the molecules are tightly bound around chlorine, carbon and hydrogen. For LOL observation in Figure 4(a) for molecules (A-D), it is noticed that the electron density distribution in the carbon-hydrogen bond is high in anisole and OCA and the delocalized electron cloud surrounding the carbon atoms. The color-filled map in Figure 4(b) for molecules (A-D) shows that the central region of all hydrogen atoms is white, which specifies the higher electron density, and bonds are dominated by a single localized orbital (exceeds the upper limit of 0.8). The high LOL values of the covalent type of electron depletion region around the hydrogen atoms are marked in red, and blue circles indicate electron depletion between the valence and inner shells of all carbon and chlorine atoms. Red circles between carbon-carbon atoms show covalent bonds [26]. In Figure 4(c), for molecules (A-D), the methoxy group creates a region of high electron localization around the oxygen atom, while the chlorine atom influences localization patterns near the ortho, meta, and para positions on the ring. Hydrogen exhibits lower electron localization compared to carbon, oxygen, and chlorine atoms. More complex counter patterns are observed near the ortho position in molecule (B), but uniformly spaced counters around the ring and at the chlorine position (meta) are seen in molecule (C), and closely spaced counters appear around the para position in molecule (D). The black ring around oxygen atoms indicates the lone pair, and around carbon atoms indicates the bonding electron pair. Likewise, a double ring around the chlorine atom in molecules (B), (C), and (D) indicates the presence of a lone pair and high electron localization in that area.

4.4. Analysis of molecular electrostatic potentials (MEPs)

MEP is useful to illustrate the charge distributions of molecules and is used to visualize variably charged regions of a molecule [27]. It is a 3D plot of electrostatic potential mapping over the constant electron density surface and presents molecular size, shape, and electrostatic potential value [28].

The increase in electrostatic potential value represents blue color, while the red color represents a decrease in electrostatic potential value. Accordingly, red represents the regions of the most negative electrostatic potential, and blue represents the region of poor electron (i.e., the most electropositive region), as the potential increases in the order red < orange< yellow< green < blue [29].

Figure 5(a), (b), (c), and (d) represent the MEP of anisole, OCA, MCA, and PCA, respectively. The transparent view for MEP is computed at 0.002 au. isodensity surface and indicates the electronegative area around the oxygen atom (red color), aromatic carbon atom (yellowish color), and chlorine atom at ortho, meta, para positions (orange color), which exhibit nucleophilic reaction activity. The region of hydrogen atoms is light blue and green, indicating zero potential. These sites give information about the region where the compound can have non-covalent interactions [29]. From MEP, it is evident that the most electropositive region is located over the C-H bond for all the molecules, and the most electronegative region is located over the oxygen bonded to carbon for the anisole molecule. While in the OCA, MCA and PCA, the most electron-rich region is investigated over the chlorine bonded to the carbon atom of the benzene ring.

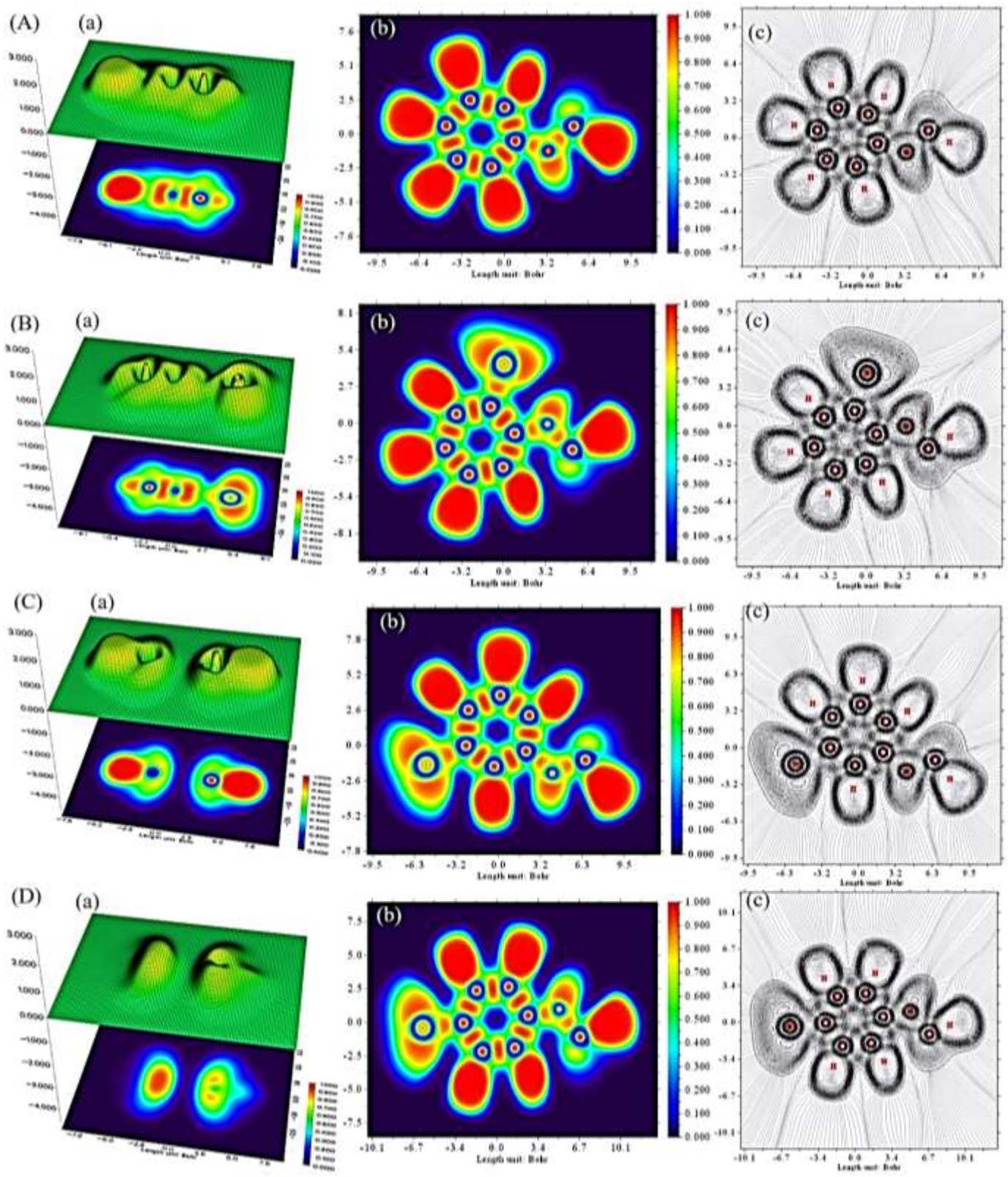

Figure 3. ELF (a) shaded surface map with the projection showing an electronic environment, (b) colored filled (c) counter map of (A) anisole, (B) OCA, (C) MCA and (D) PCA.

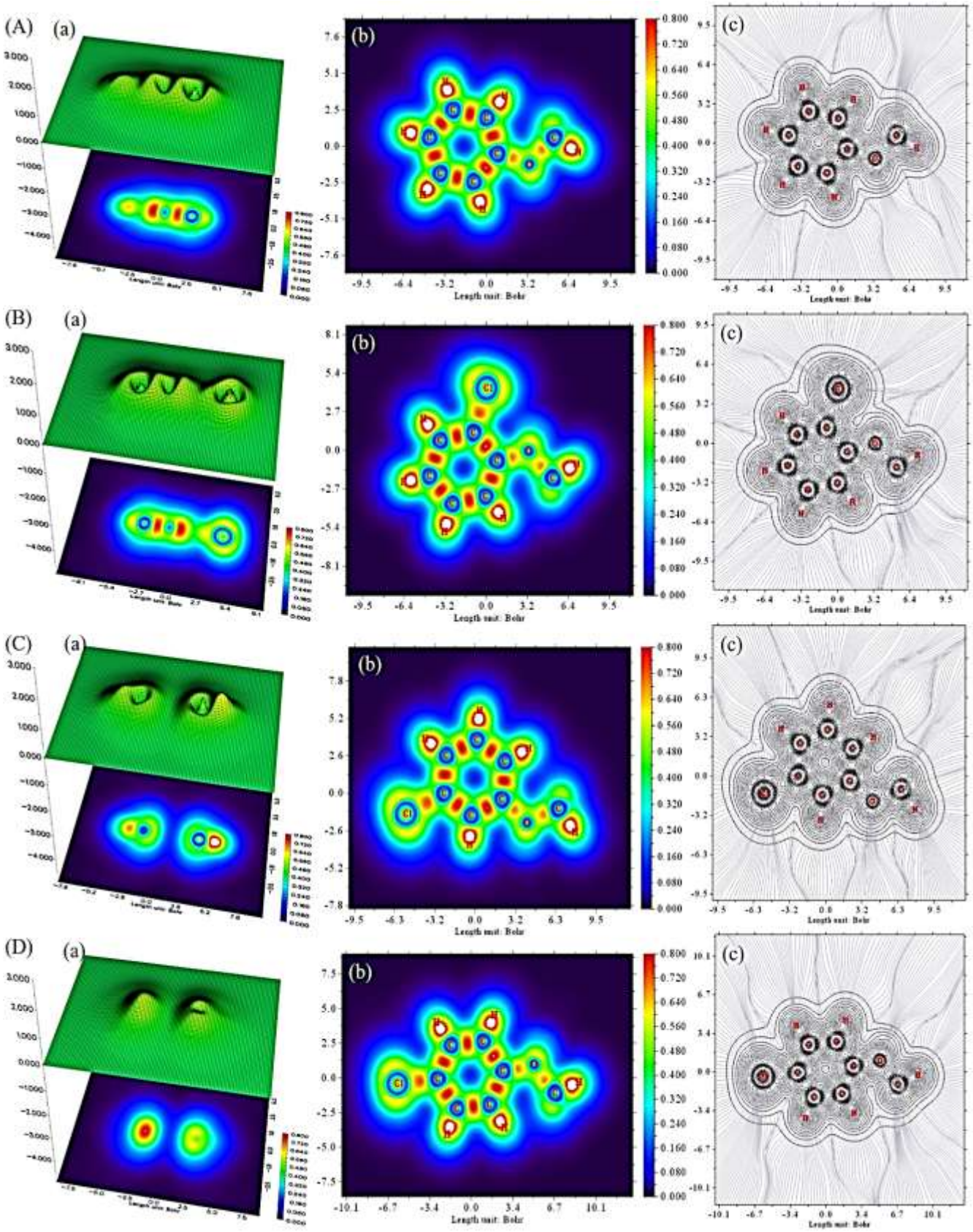

Figure 4. LOL (a) shaded surface map with the projection showing an electronic environment, (b) colored filled (c) counter map) for (A) anisole, (B) OCA, (C) MCA and (D) PCA.

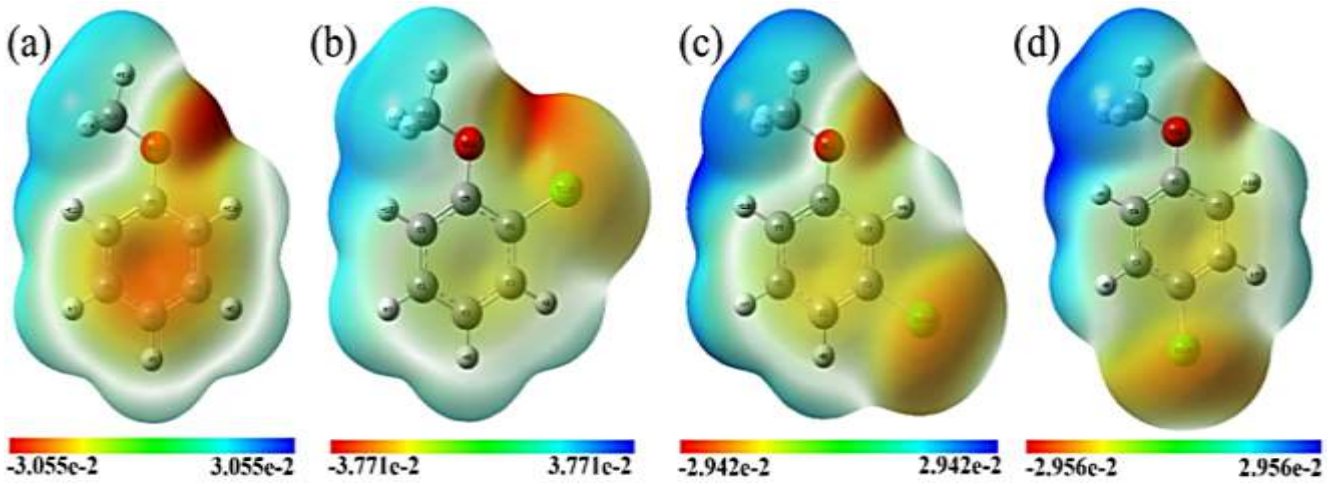

Figure 5. MEP for (a) Anisole, (b) OCA, (c) MCA and (d) PCA

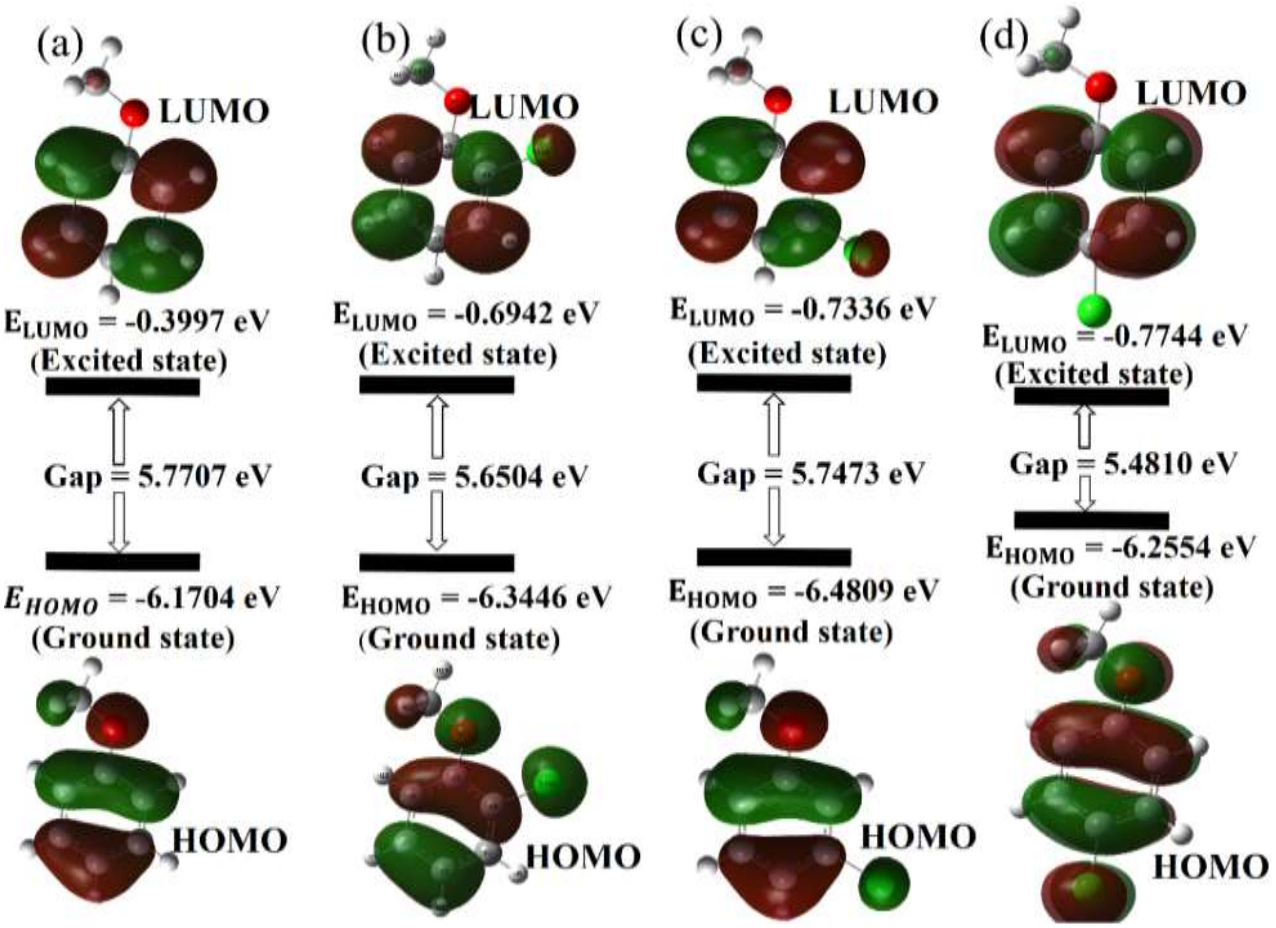

Figure 6. Frontier molecular orbital (HOMO-LUMO) views for (a) anisole, (b) OCA, (c) MCA and (d) PCA

Table 1. Comparison of global reactivity descriptors between Anisole and Chlorine-substituted anisole at ortho, meta, and para positions

Electronic properties	Anisole	OCA	MCA	PCA
Ionization potential (I)	6.1704	6.3446	6.4809	6.2554
Electron Affinity (A)	0.3997	0.6942	0.7336	0.7744
Energy gap (ΔE)	5.7707	5.6504	5.7473	5.481
Molecular Hardness (η)	2.8853	2.8252	2.8736	2.7405
Molecular Softness (S)	0.3465	0.3539	0.3479	0.3648
Electronegativity (χ)	3.2850	3.5199	3.6072	3.5149
Chemical Potential (μ)	-3.2850	-3.5194	-3.6072	-3.6072
Electrophilic Index (ω)	1.8700	2.1920	2.2640	2.3740

4.5. Frontier molecular orbital (FMO) and global

Reactivity descriptor HOMO and LUMO are important parameters for accurately assessing electron transport charge in molecular systems [30]. The energy gap between the HOMO and LUMO molecular orbitals helps to characterize the molecule's kinetic stability and chemical reactivity. Figures 6(a), (b) (c) and (d) show the calculated frontier molecular orbital energy gaps for anisole, OCA, MCA, and PCA, respectively, and indicate that the LUMO is mainly localized over the benzene ring, while the HOMO is localized over the benzene, methoxy group, and chlorine atoms. A high HOMO value is attributed to electron-donating hydrogen atoms on the ring, while a low LUMO value is due to the electron-accepting oxygen atom in the OCH_3 group. For anisole, the HOMO-LUMO gap is 5.7707 eV, indicating it is the most stable among the four molecules (anisole, OCA, MCA, and PCA). Conversely, the HOMO-LUMO gap of PCA is 5.4810 eV, which is lower than that of anisole. This is because the chlorine atoms' para position makes PCA more reactive. This suggests PCA has the highest reactivity for interacting with the surrounding media and the extended applicability over the anisole. After anisole, MCA is more stable with a gap of 5.7473 eV, larger than OCA's 5.6504 eV. This indifference in energy gap is due to the combined effect of the methoxy (electron-donating) group and the chlorine (withdrawing) atom at the ortho position, making OCA more reactive than MCA. The ionization energy (I) and electron affinity (A) are calculated from HOMO and LUMO energies with $I = -E_{HOMO}$ and $A = -E_{LUMO}$. Other global reactivity descriptors include global hardness, molecular softness, electro-negativity, chemical potential, and global electro-philicity index. These parameters, listed in Table 1, are evaluated using the HOMO and LUMO energies obtained from the optimized structures of the studied molecules. MCA exhibits the highest electro-negativity at 3.6072 eV, making it the most electro-negative among the four. PCA shows the lowest chemical hardness, indicating it is the least stable due to its lower hardness value. As hardness decreases, softness increases, so anisole, with a high molecular hardness of 2.8853 eV, is less soft, while PCA, being softer, is more responsive to electron exchange. In addition to that, a higher (μ) value and a lower (η) value suggest better electrophilicity [30]. In this study, the nucleophile (anisole) has a lower (1.8700 eV) of (ω) while PCA has a higher (2.3740 eV) of (ω), indicating that PCA is the strongest electrophile [31] among the titled molecules. Overall, the kinetic stability is increased in the order: Anisole>MCA>OCA>PCA.

4.6. Density of state (DOS)

To identify the quantum energy levels, the total energy gap from the HOMO and LUMO energies alone is insufficient. Therefore, the DOS is constructed for this investigation. The molecular states are calculated by convoluting the molecular orbital data with Gaussian curves of unit height over an energy range from -20 eV to 10 eV, with a full width at half maximum (FWHM) of 0.3 eV, using the GaussSum 3.0 program in the gas phase. This provides a pictorial representation of the molecular orbital (MO) compositions and their contributions to chemical bonding [32]. If there is a high-intensity DOS, multiple states are accessible for occupation at a given energy level. When the intensity is zero, no states are accessible. Negative energy value represents anti-bonding interactions, positive energy value represents bonding interactions, and zero energy value represents non-bonding interactions [33]. The energy gap in DOS spectra refers to a range of energy values where electronic states are absent. Figures 7(a), (b), (c), and (d) show the DOS spectra of anisole, OCA, MCA, and PCA, respectively. These energy gap values represent the precise amount of energy

required to excite electrons from the valence band into the conduction band [33]. The anisole energy band gap of 5.8324 eV is observed to be the most stable and less chemically reactive state, resulting in very low electrical conductivity. PCA's MO has the lowest energy gap (5.5546 eV), suggesting less density of states available, and is more chemically reactive due to a higher possibility of electronic transition. While comparing the energy gaps observed in the DOS spectra and HOMO-LUMO for the studied molecules, we found that they are consistent, with only a 1-2% difference in energy gap value.

4.7. Mulliken Charges

The molecular charge explanation has been based on the Mulliken atomic charge, which describes the processes of electronegativity equalization and charge transfer in chemical reactions. Mulliken atomic charge also explains how the electronic structure changes under atomic displacement [34]. The histograms of calculated Mulliken charges of anisole, OCA, MCA, and PCA are shown in Figure 8(a), (b), (c), and (d), respectively. It is observed that the C6 of anisole, C2, C4, and C6 of OCA, C4 and C6 of MCA, and C2, C4, and C6 of PCA have the positive charges, respectively, except the C5 atom in the ring that bears the negative charge due to the oxygen atom attached to it. The oxygen atoms O12 in anisole, O11 in OCA, O12 in MCA, and O15 in PCA of the studied molecules in the methoxy group have negative charges, respectively. All the hydrogen atoms have positive Mulliken charges for the corresponding molecules. Because of the larger electronegativity and electron-withdrawing nature, all atoms of oxygen and some carbon atoms attached to the methoxy group have negative Mulliken charges.

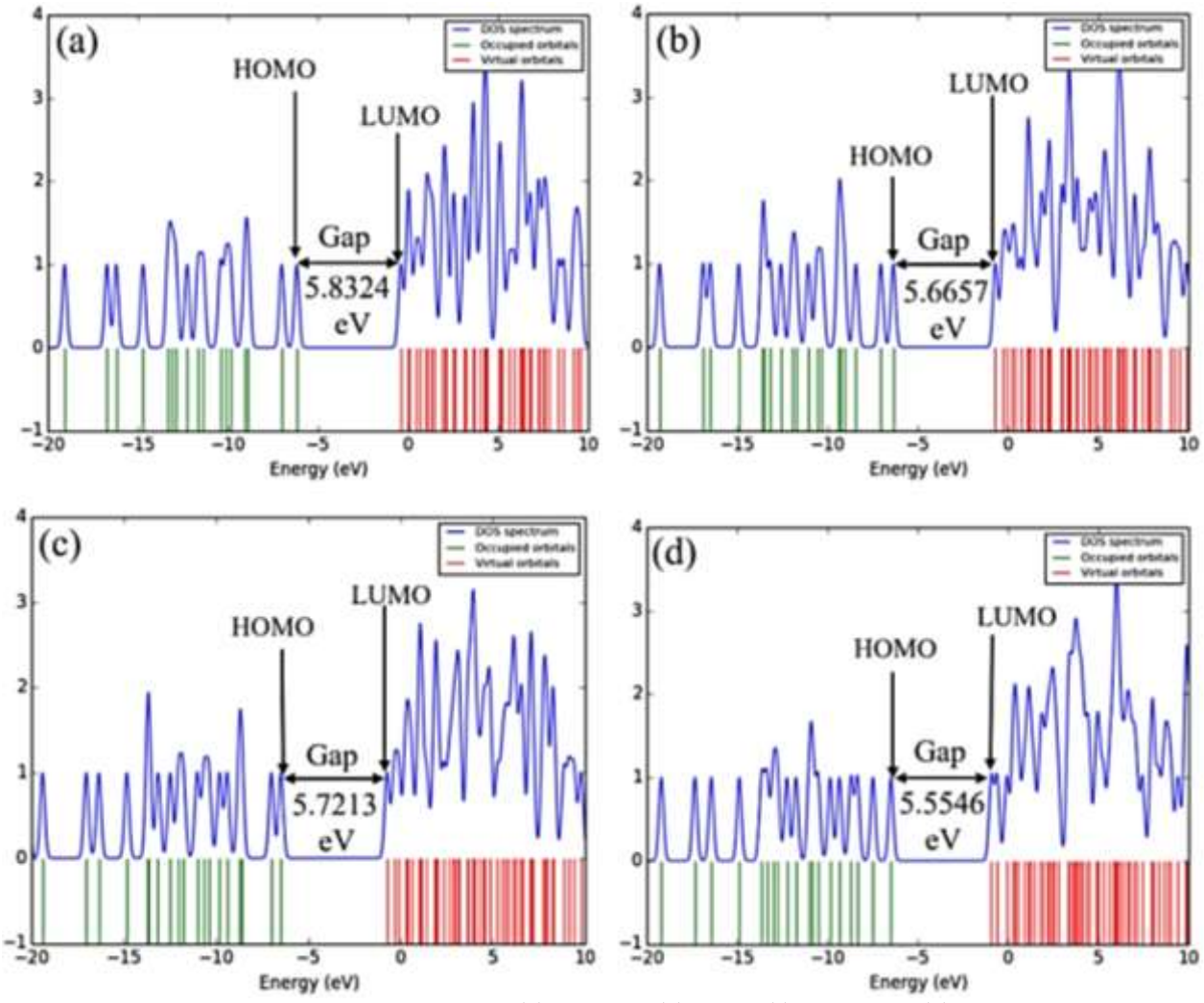

Figure 7. DOS spectrum of (a) Anisole, (b) OCA, (c) MCA and (d) PCA

The atoms Cl16, Cl11, and Cl16 of OCA, MCA, and PCA have a positive Mulliken atomic charge on the ring. The carbon atom C4 (0.798 au) of OCA has the highest positive charge, and the carbon atom C5 (-1.062 au) of the same molecule holds the highest negative charge, as illustrated in the histogram in Figure 8(b). The hydrogen atom H13 (0.155 au), which is connected to the carbon atom C12 of OCA, exhibits the highest positive charge among all the chlorine atoms at the ortho and para position.

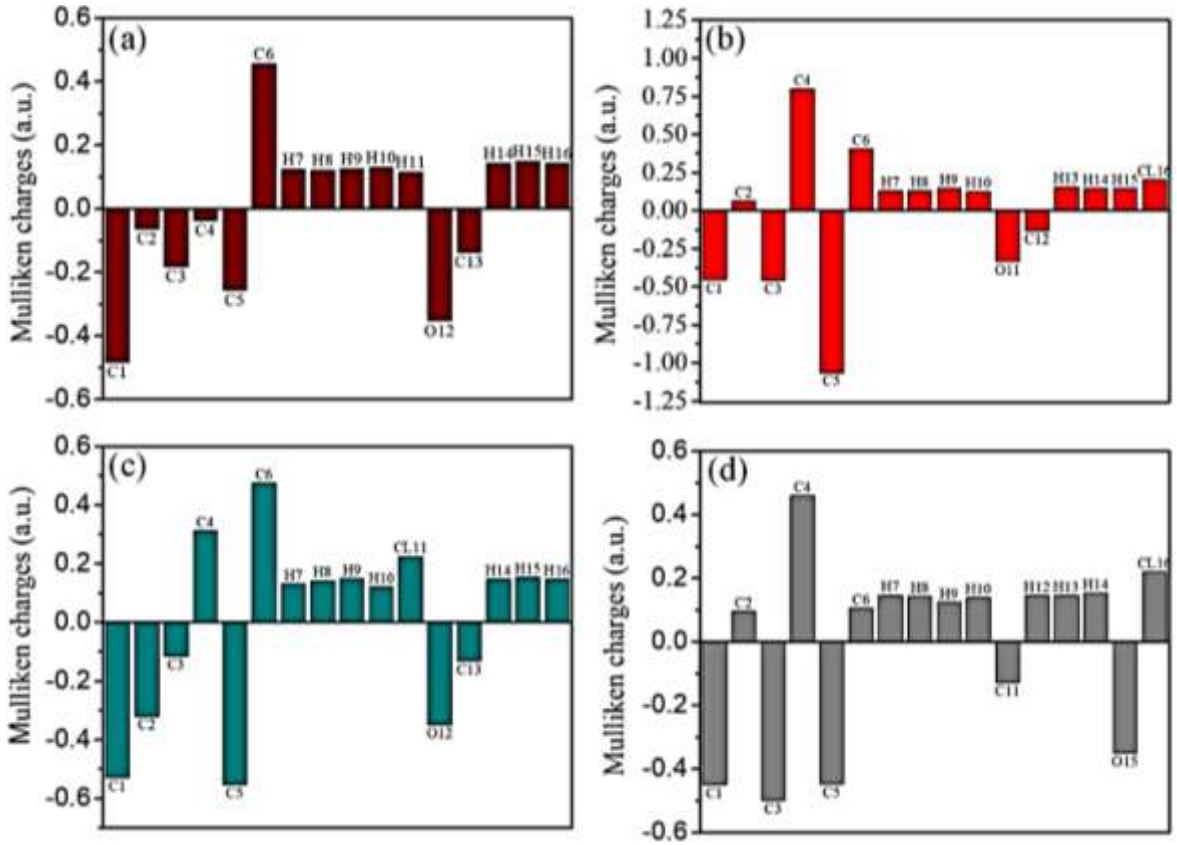

Figure 8. Atomic Mulliken charge distributions for the (a) anisole, (b) OCA, (c) MCA and (d) PCA

4.8. Vibrational Assignments

The anisole molecule consists of 16 atoms and 58 electrons, while its chlorine substituents have 16 atoms a respectively 74 electrvibration modes. The frequency versus transmittance graph for Fourier transform infrared spectroscopy (FT-IR) and the frequency versus Raman intensity graph are plotted, and various intensities for the strongest peaks are recorded. Figure 9 shows the FT-IR spectra of anisole, OCA, MCA, and PCA. It mainly shows the highest transmittance peak for C-C stretching vibration in anisole, C-C stretching, C-Cl stretching, and C-H in-plane bending vibrations, along with C-O-C stretching, and CH_3 rocking vibrations in OCA, MCA, and PCA. The vibrational spectra of the studied molecules in terms of characteristic spectral regions for the FT-IR spectroscopy are:

4.8.1. C-H vibrations

The aromatic structure shows C-H stretching vibrations in the 3100– 3000 cm^{-1}. The C-H in-plane bending vibrations appear as sharp intensity bands in the 1100–1500 cm^{-1} region [35]. The out-of-plane bending vibrations occur in the wavenumber range of 800–1000 cm^{-1} [36]. For the assignment of vibration of an anisole molecule, the aromatic C-H symmetric stretching vibrations are observed at 3017 cm^{-1}, and the in-plane C-H bending vibrations of rings at 1071 cm^{-1}. The band observed at 763 cm^{-1} is assigned to out-of-plane C-H vibrations. For the assignment of OCA, the in-plane C-H bending vibrations of rings are observed at 1505 and 1134

cm^{-1}. The bands observed at 931 and 805 cm^{-1} are assigned to out-of-plane C-H vibration. Similarly, for the assignment of MCA, the aromatic C-H stretching vibrations are observed at 3248 cm^{-1}, and the in-plane C-H bending vibrations of rings are observed at 1477, 1148, and 1050 cm^{-1}. The band observed at 819 cm^{-1} is assigned to out-of-plane C-H vibrations. Further, for the assignment of PCA, the in-plane C-H bending vibrations of rings are observed at 1491, 1134, 1085, and 1043 cm^{-1}.

4.8.2. C-C vibration

The C-C aromatic vibrations for IR spectroscopy are observed at 1600-1400 cm^{-1} [36]. Since benzene contains six equivalent C-C bonds, there will also be six C-C stretching vibrations. The bands observed at 1652 cm^{-1} of anisole are identified as C-C stretching vibrations. For OCA, the IR band for C-C vibration is observed at 1505 cm^{-1}; in MCA, the IR band at 1610 cm^{-1}, displayed in Figure 9, is called C-C modes.

4.8.3. C-Cl vibration

The vibrations in the bond between the ring and halogen atoms are worth discussing here because vibration mixing can occur due to the reduction in molecular symmetry. Usually, the C-Cl absorption appears in a broad region between 850-550 cm^{-1} [37]. A strong band at 805 cm^{-1} for OCA and 819 cm^{-1} for the MCA has been assigned to the C-Cl stretching vibration mode. For PCA, the band at 609 cm^{-1} is observed for C-Cl stretching vibrations, as shown in the spectra of Figure 9.

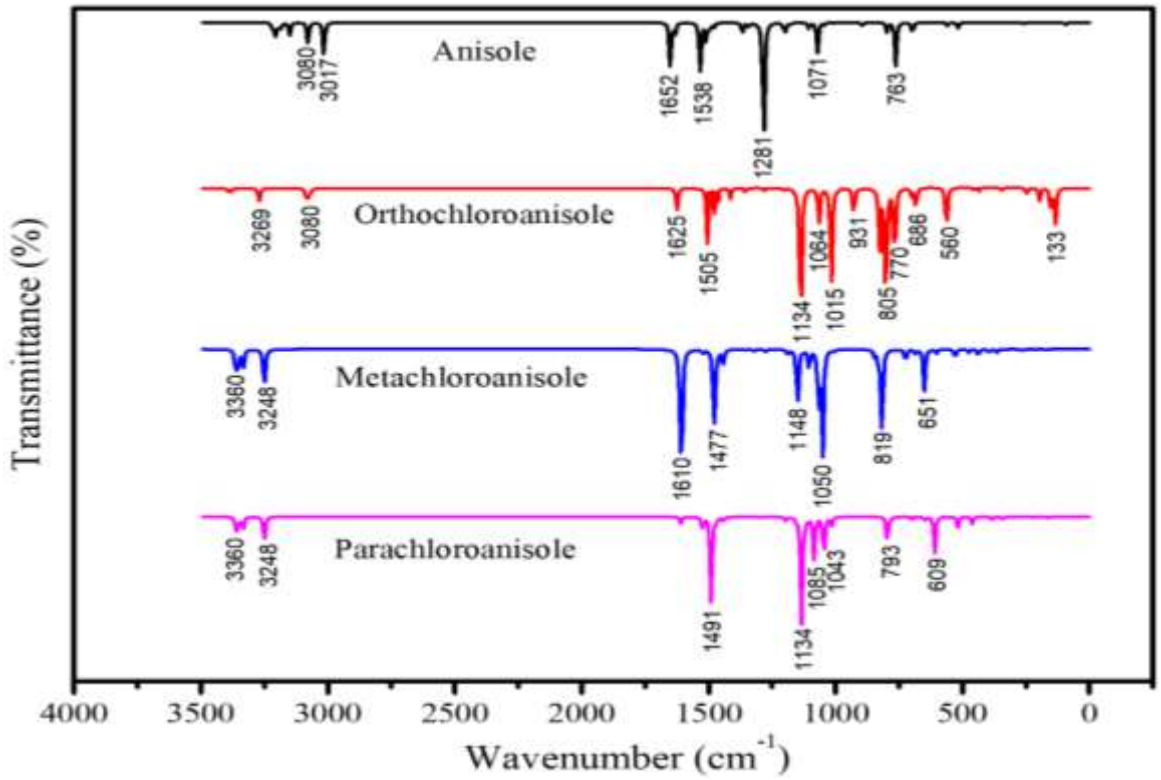

Figure 9. FT-IR spectroscopy for neutral anisole, ortho chloroanisole (OCA), meta chloroanisole (MCA) and para chloroanisole (PCA) molecules.

4.8.4. C-O-C vibration

Figure 9 of the FT-IR spectra shows the C–O–C stretching vibration for the anisole molecule at 1281 cm^{-1}. OCA shows C-O-C modes at minimum intensity band around frequency 1285.20 and 1308.19 cm^{-1} on the FT-IR spectra in Figure 9. For MCA, the stretching C-O-C vibration is observed at 1270 cm^{-1}. Likewise, the FT-IR band at 1288.08 cm^{-1} for PCA is observed to be the strongest C-O-C vibration.

4.8.5. CH_3- vibration

In aromatic compounds, the methyl CH_3 asymmetric vibrations are expected near the 3000–2925 cm^{-1} and the symmetric CH_3 vibrations in 2940–2905 cm^{-}

^{1} [38, 39]. For this work, the CH_3 asymmetric vibration in FT-IR spectra is observed at a frequency of 3080 cm^{-1}. However, the CH_3 symmetric vibration is observed at 3017 cm^{-1} for the prime molecule, anisole. For OCA, the CH_3 asymmetric vibration is observed at 3269 cm^{-1}, while the CH_3 symmetric vibration is observed at 3080 cm^{-1}. In MCA, the CH_3 asymmetric stretching mode is observed at a frequency of 3360 cm^{-1} and the CH_3 symmetric vibration at 3248 cm^{-1} in FT-IR spectra. Furthermore, CH_3 asymmetric vibration at 3360 cm^{-1} and CH_3 symmetric bands at 3248 cm^{-1} are noted for PCA. Figure 10 presents the vibrational spectra of the studied molecules, highlighting characteristic Raman spectral regions, visualized using GaussSum 3.0.

4.8.6. C-H vibrations

The weak intensity peaks are observed at 3216 cm^{-1} for aromatic C-H symmetric stretching vibrations and at 1048 cm^{-1} for the in-plane CH bending vibrations of rings for anisole in the FT-Raman spectrum. For OCA, the intensity at 3224 cm^{-1} is the aromatic C-H symmetric stretching mode, and in-plane CH bending vibrations of rings are observed at 3024 and 1064 cm^{-1}. For MCA, the frequency at 3232, 3024 cm^{-1} is observed as a C-H vibration, and the in-plane CH bending vibrations occur at 1504 and 1008 cm^{-1} in the FT-Raman spectrum, as shown in Figure 10. For PCA, the band at 3224 cm^{-1} is the C-H mode, and the in-plane C-H bending vibrations of rings are observed at the bands of 816 cm^{-1} in the FT-Raman spectrum.

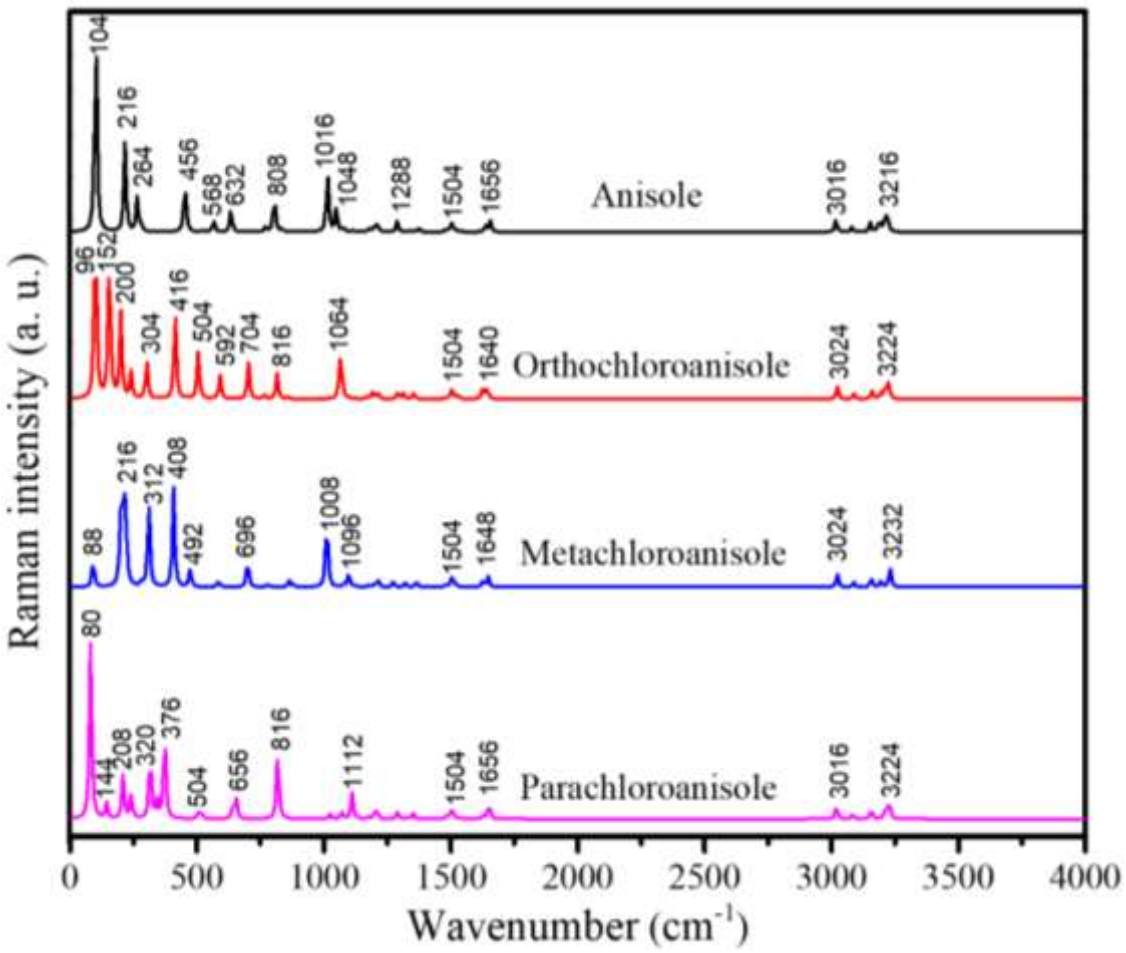

Figure 10. Raman spectroscopy for neutral anisole, OCA, MCA and PCA

4.8.7. C-C vibration

The bands observed at 1656 cm^{-1} in the FT-Raman spectrum of anisole are identified as C-C stretching vibrations. For OCA, MCA, and PCA, the Raman bands at 1640 cm^{-1}, 1648 cm^{-1}, and 1658 cm^{-1}, respectively, are the C-C modes of vibrations.

4.8.8. C-Cl vibration

In Raman Spectra, the band identified at 704 cm^{-1} for OCA is the C–Cl stretching mode. For the MCA, a strong stretching band has been established at 408 cm^{-1} and for the PCA, a band at 1112 cm^{-1} is observed to be C-Cl stretching modes of vibration in Figure 10.

4.8.9. C-O-C vibration

C-O-C mode appears at 1288 cm^{-1} in the Raman spectrum for anisole. For OCA, MCA, and PCA, the stretching C-O-C vibrations show up as a weak band around 1250-1500 cm^{-1} in Figure 10 of the Raman spectra.

4.8.10. CH_3- vibration

The CH_3 asymmetric vibration in Raman spectra is usually found at 3216 cm^{-1}. However, CH_3 symmetric vibrations are observed at 3016 cm^{-1} in Raman spectra for the anisole molecule. For OCA, CH_3 asymmetric vibrations are observed at 3224 $cm^{-1,}$ while CH_3 symmetric vibrations are observed at 3024 cm^{-1}. For MCA, CH_3 asymmetric and symmetric stretching modes are observed at a frequency of 3232 and 3024 $cm^{-1,}$ respectively. Furthermore, CH_3 asymmetric vibration at 3224 cm^{-1} and symmetric bands at 3016 cm^{-1} are noted for PCA. Furthermore, the characteristic spectra, Raman inten
aks, observed in Figure 10, anisole shows the highest Raman intensity peaks between 0-1016 cm^{-1} of frequency, 0-1064 cm^{-1} of frequency for OCA, 0-1008 cm^{-1} of frequency for MCA, and 0-816 cm^{-1} of frequency for PCA.

4.9. UV-Vis analysis

The ultraviolet-visible (UV–Vis) analysis of the title compounds is conducted using Time-Dependent Density Functional Theory (TD-DFT) to analyze the spectra in a neutral state [40]. The maximum wavelengths of the studied molecules vary significantly, as shown in the UV-Vis spectra in Figure 11(a), (b), (c), and (d). All molecules exhibit UV–Vis absorption in the range of 200–300 nm at a neutral state. Figures 11(a) through (d) indicate that the spectral intensity of all molecules drops to zero at wavelengths greater than 300 nm. The maximum wavelength (λmax) for the anisole molecule is 246.5 nm, with oscillator strengths of 0.0346, an excitation energy of 9431.82 eV, and a dipole moment of 1.397160 Debye. Similarly, the λ_{max} values for the chlorine-substituted anisole derivatives—OCA, MCA, and PCA- are observed at 251.5 nm, 249.5 nm, and 224.2 nm, with oscillator strengths of 0.0487, 0.0331, and 0.0339, respectively, and excitation energies of 21938.03, 21938.08, and 21938.24 eV. PCA shows the shortest wavelength compared to the other compounds, while OCA exhibits the longest, suggesting that this molecule absorbs light most effectively. These variations in wavelength and intensity are due to differences in electron transition interactions involving the chlorine atom at the ortho, meta, and para positions.

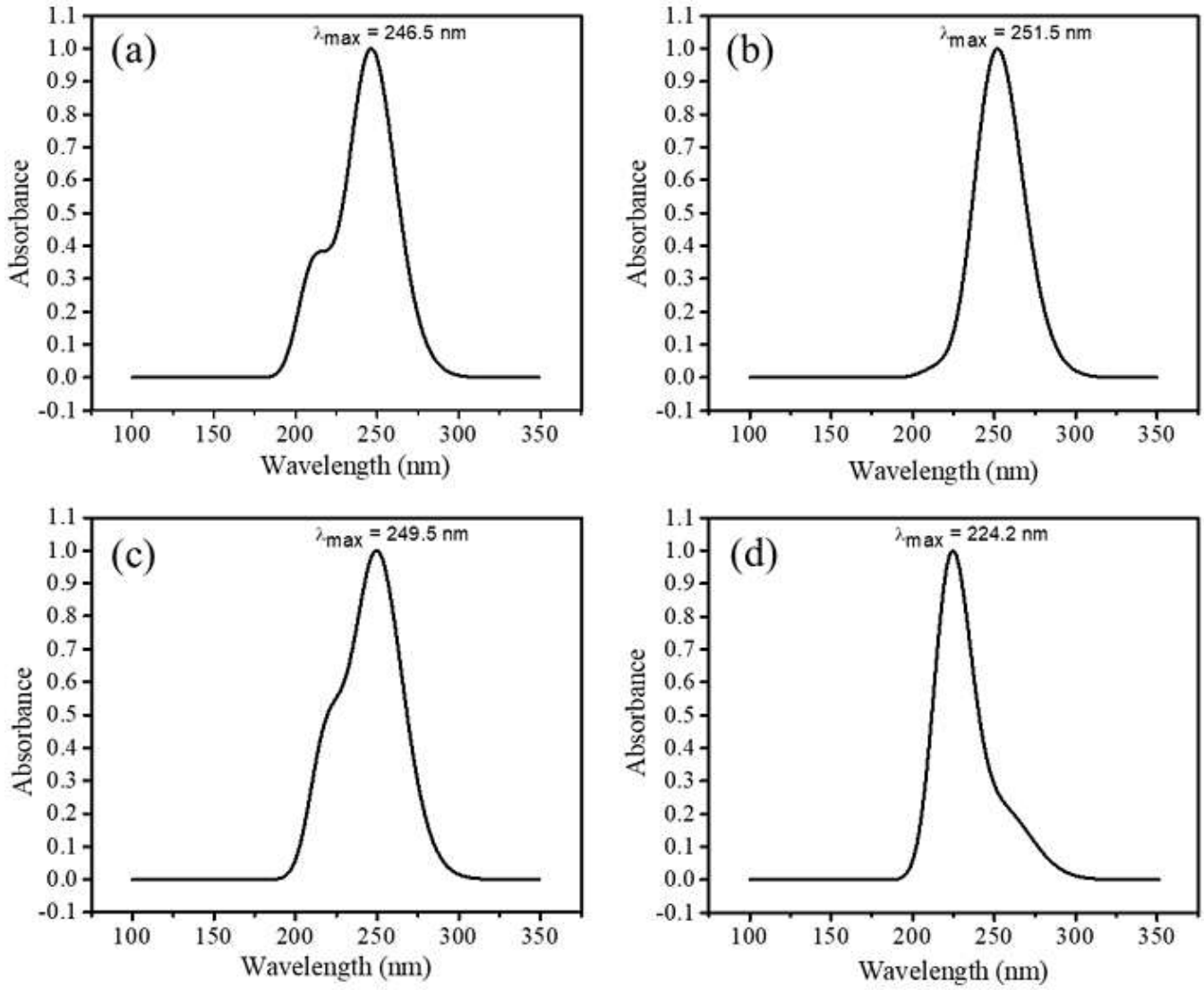

Figure 11. UV-Vis spectrum of the (a) Anisole, (b) OCA, (c) MCA and (d) PCA

4.10. Thermodynamic properties

Different thermodynamic parameters, such as enthalpy, Gibbs free energy, and entropy, evaluate the state and direction of a chemical reaction. These parameters also describe the spontaneity of a reaction and its energy profile (endothermic or exothermic) and the temperature effects on various thermodynamic properties [41]. Figure 12(a), (b), (c), and (d) with quadratic fitting demonstrate the positive correlation of heat capacity at constant pressure (C_p), enthalpy (H), and entropy (S) versus increase in temperature for anisole, OCA, MCA and PCA, respectively. The correlation equations [42] shown in Figure 12(a) reflect the second-order polynomial fit between the thermodynamic quantities and the temperature for C_p, H, and S of anisole, with the corresponding R^2 values of 0.99727, 0.99991, and 0.98448, respectively. Figure 12(b) shows a graph of thermodynamic parameters for temperature and their correlation equations from a quadratic fit for OCA. The resulting correlation models yielded coefficients of determination (R^2) of 0.99871, 0.99999, and 0.98972 for C_p, H, and S, respectively, indicating an excellent fit. Figure 12(c) shows a positive correlation between temperature and the thermodynamic properties with second-order polynomial fits yielding R^2 values of 0.9985, 0.99999, and 0.98982 for C_p, H, and S, respectively. In Figure 12(d), the second-order polynomial fits between thermodynamic properties and temperature of MCA

yielded R^2 values of 0.99881 for C_p, 0.99999 for H, and 0.9892 for S, respectively. It is observed for all the molecules that C_p, H, and S increase with increasing temperature. Here, the entropies (S) for all the given molecules sharply increase, and all the heat capacities at constant pressure (C_p) moderately rises with the increase in temperature from 10 K to 500 K. However, the enthalpy (H) increases very slowly with the same rise in temperature.

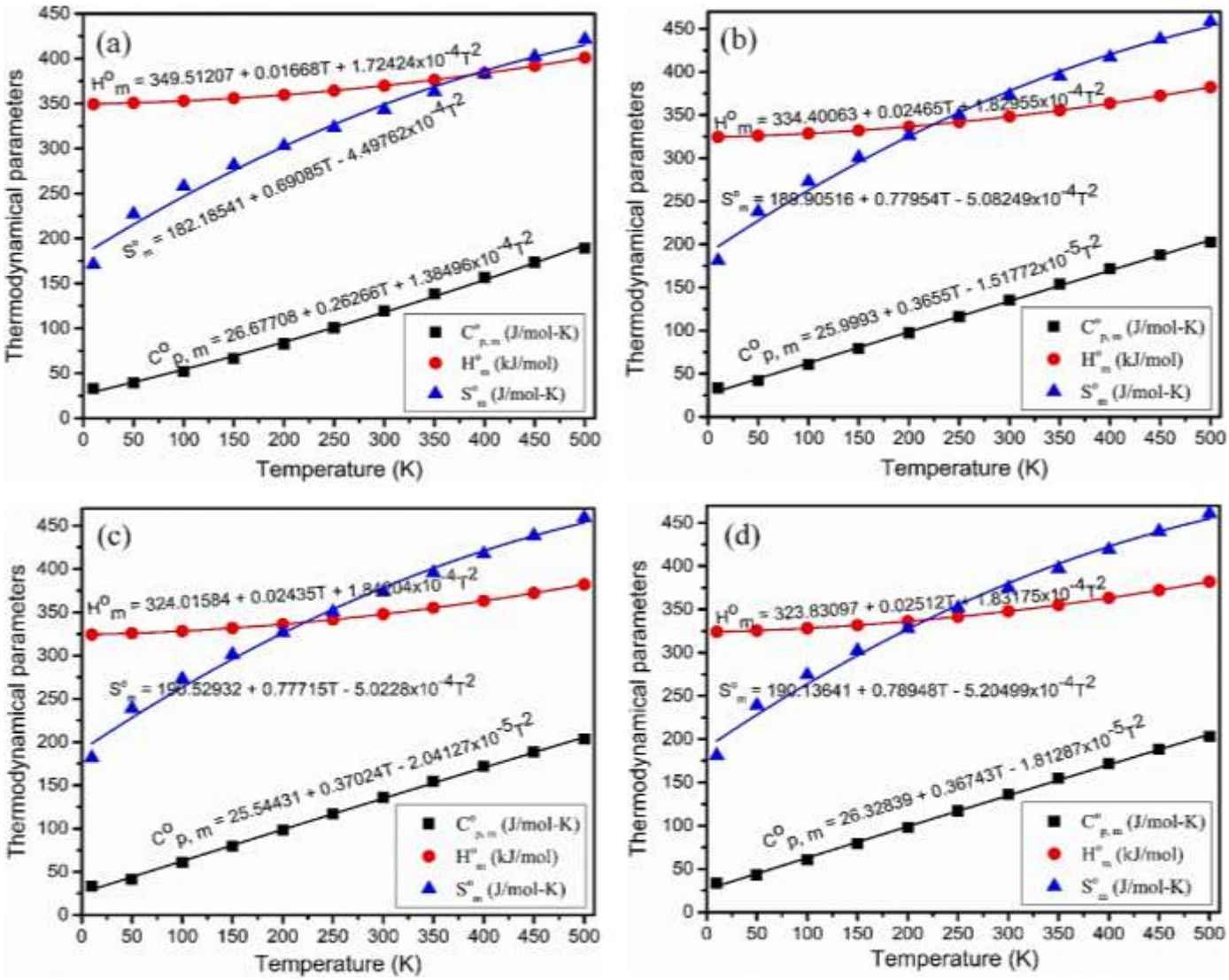

Figure 12. Correlation plot for thermodynamic properties at different temperatures for (a) anisole, (b) OCA, (c) MCA, and (d) PCA.

5. Conclusion

Quantum calculations and spectroscopic analysis were conducted computationally using the B3LYP/DFT method with 6-31+G(d,p) basis set, and comparisons were made for anisole, OCA, MCA, and PCA. The results of the comparison were found to be contradictory and fluctuating regarding the electronic structure, charge transfer in chemical reactions, the reactivity-stability relationship, NCI-RDG plots, the processes of electronegativity equalization, and the concepts of chemical hardness and softness, as well as vibrational spectroscopy of the targeted compounds. Anisole is identified as the most stable compound and demonstrates lower reactivity. In contrast, PCA is

more likely to exchange electrons and exhibit the highest reactivity in interactions with surrounding atoms or molecules. For the MEPs, the negative potential sites are located on chlorine, oxygen, and carbon atoms, while the positive potential sites are around the hydrogen atoms and the surrounding region. The presence of substituted chlorine in anisole decreases the stability due to its electronegative and reactive nature. Van der Waals interactions are the dominant forces in the PCA molecule. Ultraviolet-visible absorbance spectra calculations show that the maximum peak is observed at 251.5 nm for OCA. The impact of chlorine is significant, affecting not only the immediate environment of the substitution site but also other areas of the aromatic ring. The substitution of chlorine in the ring results in notable changes in the ring stretching modes, in-plane bending modes, and out-of-plane bending modes of the OCA, MCA, and PCA molecules. Inconsistencies such as the increasing values of heat capacity (C_p), enthalpy (H), and entropy (S) are observed among the studied molecules due to temperature variations. To sum up, this research can either assist in selecting the appropriate form of anisole and its derivatives for specific applications or help distinguish between anisole and its chlorinated derivatives. Future work should include experimental findings with solvent phase calculations. This work will help us better understand how to design halogenated aromatics with the right balance of reactivity and stability for real-world uses like medicines, crops, and advanced materials.

Acknowledgment: Authors are thankful to the Department of Physics, St. Xavier's College, Kathmandu, for providing computational assistance for this work.

Conflicts of Interest: There are no conflicts of interest.

Funding statement: This work received no external funding.

References

[1] Dionisio, K.; Phillips, K.; Price, P.; "The Chemical and Products Database, a resource for exposure-relevant data on chemicals in consumer products". Sci Data., 5: 180125, 2018.

[2] Vani, B.; Pabba, M.; Kalyani, S., Kalyani, S.; Sridhar, S.; "Separation of Anisole and Valuable Byproducts from Liquid Reaction Mixtures by Solvent Extraction and Multicomponent Distillation". J. Solution Chem., 50: 160–177, 2021.

[3] El-Saady, A. A.; Roushdy, N.; Farag, A. A. M.; "Exploring the molecular spectroscopic and electronic characterization of nanocrystalline Metal-free phthalocyanine: A DFT investigation". Opt. Quantum Electron., 55, 662, 2023.

[4] Ayachi, S.; Bergaoui, S.; Ben Khalifa, I.; Haj Said, A.; Chemek, M.; "On the photo-physical properties of soluble oligomer from anodic oxidation of chlorine-substituted anisole (OPClAn)". Synth. Met., 166: 22, 2013.

[5] Malongwe, J.; K. E., Nachtigallová, D.; Corrochano, P.; and Klán, P.; "Spectroscopic Properties of Anisole at the Air–Ice Interface: A Combined Experimental–Computational Approach". Langmuir, 32(23): 5755-5764, 2016.

[6] Ali, M.; Mansha, A.; Asim, S.; Zahid, M.; Usman M., et al.; "DFT Study for the Spectroscopic and Structural Analysis of p-Dimethylaminoazobenzene". J. Spectroscopy, 2018: 1-15, 2018.

[7] Shastri, A.; Das, A. K.; Rajasekhar, B. N.; "The electronic absorption spectrum of Anisole was studied by photo absorption spectroscopy and quantum chemical calculations". J. Quant. Spectrosc. Radiat Transfer, 242: 2020.

[8] Frisch, M.J.; Trucks, G. W.; Schlegel, H. B.; Scuseria, G. E.; Robb, M. A.; et al.; Gaussian 09, Gaussian, Inc., Wallingford, CT, 2009.

[9] Dennington, R.; Keith, T. A.; Millam, J. M.; GaussView, version 6.0. 16., Semichem Inc, Shawnee Mission, 2016.

[10] Jana, S.; Samal, P.; "Assessment and Benchmarking of Proposed Exchange-Correlation Approximations in Density Functional Theory". Doctoral dissertation, School of Physical Sciences, NISER, Bhubaneswar, 2021.

[11] Nagy, B.; Jensen, F.; "Basis sets in quantum chemistry". Rev. Comput. Chem., 30: 93-149, 2017

[12] Ignatov, S. K.; Moltran v.2.5 - Program for molecular visualization and thermodynamic calculations. Uni. of Nizhny Novgorod, 2004.

[13] O'Boyle, N. M.; Tenderholt, A. L.; Langner, K. M.; "A library for package-independent computational chemistry algorithms". J. Comput. Chem., 29(5): 839–845, 2008.

[14] William, H.; Andrew, D.; Klau, S.; VMD - Visual Molecular Dynamics, J. Mol. Graphics., 14: 33-38, 1996

[15] Johnson, E.R.; Keinan, S.; Mori-Sánchez, P.; Contreras-García, J.; Cohen, A.J.; Yang, W.; "Revealing noncovalent interactions". J. Am. Chem. Soc., 132(18): 6498-506, 2010

[16] Lu, T.; Chen, F.; "Multiwfn: A Multifunctional Wavefunction Analyser". J. Comput. Chem. 33: 580-592, 2012

[17] Ylivainio, K. J.; Sufyan, A.; Larsson, J. A.; "A quantitative relationship between electron localization function and the strength of physical binding". J. Phy.: Condens. Matter., 37(20); 205502, 2025.

[18] Kores, J. J.; Danish, I. A.; Sasitha, T.; Stuart, J. G.; Pushpam, E. J.; Jebaraj, J. W.; "Spectral, NBO, NLO, NCI, aromaticity and charge transfer analyses of anthracene-9, 10-dicarboxaldehyde by DFT". Heliyon, 7(11), 2021.

[19] Murray, J. S.; Politzer, P.; "The electrostatic potential: an overview. Wiley Interdisciplinary Reviews". Comput. Mol. Sci., 1(2): 153–163, 2011.

[20] Bishwokarma, N.; Budha, C.; Teemilsina, N. K.; Rai, K. B. "Exploring vibrational spectra, electronic properties and thermal analysis of Isoguanine molecule using DFT". Scientific World, 18(18): 5–14, 2025.

[21] Assad, H.; Thakur, A.; Sharma, A. K.; Kumar, A.; "Density functional theory-based molecular modeling. In Computational Modelling and Simulations for Designing of Corrosion Inhibitors". Elsevier, 95-113, 2023

[22] Contreras-García, J.; Johnson, E. R.; Keinan, S.; Chaudret, R.; Piquemal, J. P.; et al. "NCIPLOT: A Program for Plotting Noncovalent Interaction Regions". J. Chem. Theory Comput., 7: 625-632, 2011.

[23] Johnson, E. R.; Keinan, S.; Mori Sanchez, P.; Contreras-Garcia, J.; Cohen, A. J.; et al.; "Revealing Noncovalent Interactions". J. Am. Chem. Soc., 132: 6498-6506, 2010.

[24] Saleh, G.; Gatti, C.; Presti, L. L.; "Non-covalent interaction via the reduced density gradient: Independent atom model vs experimental multipolar electron densities". Comput. Theor. Chem., 998: 148-163, 2012.

[25] Janani, S.; Rajagopal, H.; Muthu, S.; Aayisha, S.; Raja, M.; "Molecular structure, spectroscopic (FT-IR, FT-Raman, NMR), HOMO-LUMO, chemical reactivity, AIM, ELF, LOL and Molecular docking studies on 1-Benzyl-4-(N-Boc-amino) piperidine" J. Mol. Struct., 1230: 129657, 2021

[26] Dhanalakshmi, E.; Rajesh, P.; Arunkumar, K.; Gnanasambandan, T.; Issaoui, N.; Sudha, K.; Raja, M.; "Synthesis, GCMS, spectroscopic, electronic properties, chemical reactivity, RDG, topology and biological assessment of 1-(3, 6, 6-trimethyl-1, 6, 7, 7a-tetrahydrocyclopenta [c] pyran-1-yl) ethenone". Chem. Phys. Impact., 7: 100385, 2023.

[27] Gharti Magar, P.; Uprety, R.; Rai, K. B.; "First-principles DFT study of the molecular structure, spectroscopic analysis, electronic structures, and thermodynamic properties of ascorbic acid". Himal. Phys., 11: 28-40, 2024.

[28] Yankova, R.; Genieva, S.; Halachev, N.; Dimitrova, G.; "Molecular structure, vibrational spectra, MEP, HOMO-LUMO and NBO analysis of $Hf(SeO_3)(SeO_4)(H_2O)4$". J. Mol. Struct., 1106: 82-88, 2016.

[29] Ojha, T.; Limbu, S.; Shrestha, P. M.; Gupta, S. P.; Rai, K. B.; "Comparative Computational Study on Molecular Structure, Electronic and Vibrational Analysis of Vinyl Bromide based on HF and DFT Approach". Himal. J. Sci. Technol., 7(1): 38–49, 2023.

[30] Limbu, S.; Ojha, T.; Ghimire, R. R.; Rai, K. B.; "An investigation of vibrational analysis, thermodynamic properties, and electronic properties of Formaldehyde and its stretch by substituent acetone, acetyl chloride, and methyl acetate using first principles analysis". BIBECHANA, 21(1): 23–36, 2024.

[31] Vincy, C. D.; Tarika, J. D.; Dexlin, X. D.; Rathika, A.; Beaula, T. J.; "Exploring the antibacterial activity of 1, 2-diaminoethane hexanedionic acid by spectroscopic, electronic, ELF, LOL, RDG analysis, and molecular docking studies using the DFT method". J. Mol. Struct., 1247: 131388, 2022.

[32] Hajam, T. A.; Sallem, H.; Padhusha, M. S. A.; Mohammed Ameen, K. K.; "Synthesis, quantum chemical calculations and molecular docking studies of 2-ethoxy-4[(2-trifluoromethyl-phenylimino) methyl] phenol". Mol. phys., 118(1):1-19, 2020.

[33] Mandal, S.; Reber, A. C.; Qian, M.; Weiss, P. S.; Khanna, S. N.; Sen, A.; "Controlling the band gap energy of cluster-assembled materials". Acc. Chem. Res., 46(11): 2385-2395, 2013.

[34] Rai, K. B.; Ghimire, R. R.; Dhakal, C.; Pudasainee, K.; Siwakoti, B.; "Structural Equilibrium Configuration of Benzene and Aniline: A First-Principles Study". J. Nepal Chem. Soc., 44(1): 1–15, 2024.

[35] Ahluwalia, V. K.; "Instrumental Methods of Chemical Analysis". 1st ed.; Springer, Cham, Switzerland, 2023.

[36] Arivazhagan, M.; Jeyavijayan, S.; "Vibrational spectroscopic, first-order hyperpolarizability and HOMO, LUMO studies of 1, 2-dichloro-4-nitrobenzene based on Hartree–Fock and DFT

calculations". Spectrochim. Acta, Part A 79(2): 376-383, 2011.

[37] Sangeetha, T.; Dineshkumar, P.; Shanmugam, R.; Elangovan, A.; Arivazhagan, G.; "Hydrogen bond complexation of ethanol with chlorobenzene: FTIR studies". Phys. Chem. Liq., 63(1): 1-12, 2025.

[38] Karaca, Ç.; "Spectroscopic (FT-Raman, FT-IR, UV-Vis, and NMR) and Theoretical Analysis of 1-Methylindole: Structural Characterization, Non-Covalent Interactions, and Electronic Properties". Celal Bayar U. J. Sci., 21(1): 35-49, 2025.

[39] Faizan, M.; Bhat, S. A.; Alam, M. J.; Afroz, Z.; Ahmad, S.; "Anharmonic vibrational and electronic spectral study of 2-amino-4-hydroxy-6–methylpyrimidine: A combined experimental (FTIR, FT-Raman, UV–Vis) and theoretical (DFT, MP2) approach". J. Mol. St., 1148: 89-100, 2017.

[40] Rijal, R.; Sah, M.; Lamichhane, H. P.; "Molecular simulation, vibrational spectroscopy, and global reactivity descriptors of pseudoephedrine molecule in different phases and states". Heliyon, 9(3): e14801, 2023.

[41] El-Bindary, A. A.; Mohamed, G. G.; El-Sonbati, A. Z.; Diab, M. A.; Hassan, W. M. I.; Geometrical structure, potentiometric, "molecular docking and thermodynamic studies of azo dye ligand and its metal complexes". J. Mol. Liq., 218: 138-149, 2016.

[42] Uprety, R.; Ghimire, R.; Gharti Magar, P.; Rokka, D.; Khadka, I. B.; Neupane., R.; Rai, K. B.; "Study of the molecular structure, electronic structure, spectroscopic analysis and thermodynamic properties of dibenzofuran using first principles". J. Nepal Chem. Soc., 10(2): 8–18, 2024.